Innovations in Super-Resolution Microscopy

Innovations in super resolution microscopy

Sciammarella C.A.[a], Lamberti L[b], Santoro L[b], Sciammarella F.M.[c]

[a] *Department of Mechanical, Materials and Aerospace Engineering, Illinois Institute of Technology, 10 SW 32nd St., 60616, Chicago, IL USA*
[b] *Dipartimento Meccanica, Matematica e Management, Politecnico di Bari*, *Viale Orabona4, 70125, Bari, Italy*
[c] *MXD Corporation, 1415 N. Cherry Avenue, Chicago, IL 60642, USA*

Abstract
Viruses are organisms that to reproduce utilize cells of living beings that they invade. They consist of nucleic acids, RNA, underlying proteins, and a protective membrane. Their life cycle comprises three main stages:1)penetration of a cell, b) introduction of their genome generating new viruses,3) release of replicated viruses to the external cellular space for further infection propagation. Imaging techniques provide an important tool for understanding these mechanisms. Transmission electronic microscopy(TEM) is one of the main tools utilized for this purpose. TEM investigations impose environmental limitations to the observation conditions. To get images of viruses a TEM requires freezing the virus at extremely low temperatures. The bulk of TEM images are limited to 2D, for 3-D images TEM holography is available but poses additional difficulties and costs.
A nano-microscope is being developed with resolution limits in the same range than a TEM. The nano-microscope can be utilized to observe viruses under environmental conditions in the range of biological entities and it makes possible 3D dynamic observations.

1.Introduction
The word holography was coined by D. Gabor to label an imaging technique with the capacity of encoding 3D spatial information in 2D, by recording not only the light intensity of a wavefront but also the phase of the captured wavefront. The name Moiré-Holography was introduced as a designation of a method that has capability of recording intensity and phase utilizing the moiré technique [1]. Gratings are introduced in the optical system to produce moiré patterns that contain thein-plane and the out-of-plane information. An alternative technique introduced in which holography and moiré are applied is called holographic moiré [2] that is discussed in detail in [2] and enclosed references.
This paper presents a nano-microscope using moiré-holography as the tool to encode spatial information in the nanometric range. In [3], was introduced a methodology to obtain images of viruses with spatial resolutions in the same order of magnitude than transmission electron microscopy (TEM) utilizing light in the range of frequencies that go from ultraviolet to visible near-infrared (i.e. wavelengths from 300 up to roughly 900's nm).
Fig. 1 shows the device that supports the proposed methodology.The nano-microscope consists of a) digital microscope, b) illumination and light conditioning system, c) desktop processor, d) display monitor.
The digital microscope is connected to a desktop processor that contains the software required to 1) image acquisition,2) image preprocessing,3) Artificial intelligence neural network to classify images, 4) presentation of the results.
The illumination system consists of a laser diode that produces a laser light that will generate evanescent illumination wavefronts, a prism that will steer the beam to produce evanescent wavefronts. The observed objects are contained in a standard depression well slides that include a liquid saline solution. The illumination system contains two important components. A grating that is at the top of the prism and supports the depression well slide, and a ball lens that forms part of the microscope optical circuit as shown in Fig. 1.
Fig. 2(a) shows the ball lens that forms part of the microscope circuit. In the experiments leading to the design of the microscope, the ball lens was a polystyrene sphere of diameter 6 microns. The ball lens was fixed to the microscope slide surface to ensure that it will not move. The ball lens has a dual role in the microscope, it captures the wavefronts emitted by the observed object at the same time generates Bessel wavefronts that can propagate through the optical circuit to the image plane without experiencing diffraction, thus makingpossible observation of the near optical field in the far field. The grating indicated in Figs. (1) and (2) encodes the metrological information in the formed images.
Fig. 2(a) shows an expanded view of the region of the microscope that contains the observed objects

Fig. 2b(1) shows a prismatic nanocrystal; 2b(2) shows wavefronts entering and emerging from the ball lens acting as a relay lens;2b(3) shows wavefronts arriving at the focal plane of the spherical lens;2b(4) shows the wavefronts arriving at the image plane of the CCD.

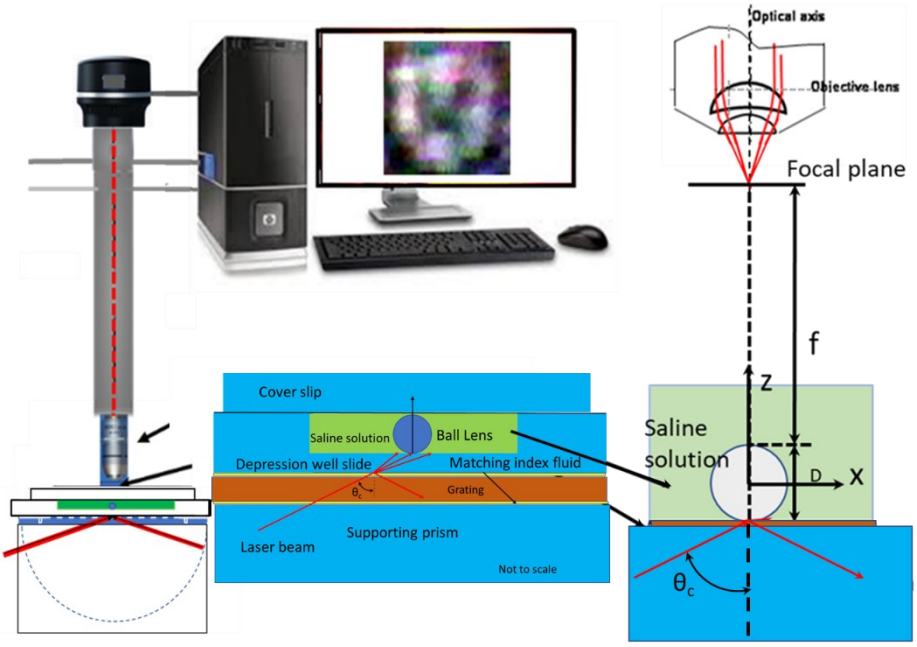

Fig. 1. Schematic representation of the nano-microscope set up proposed in this research.

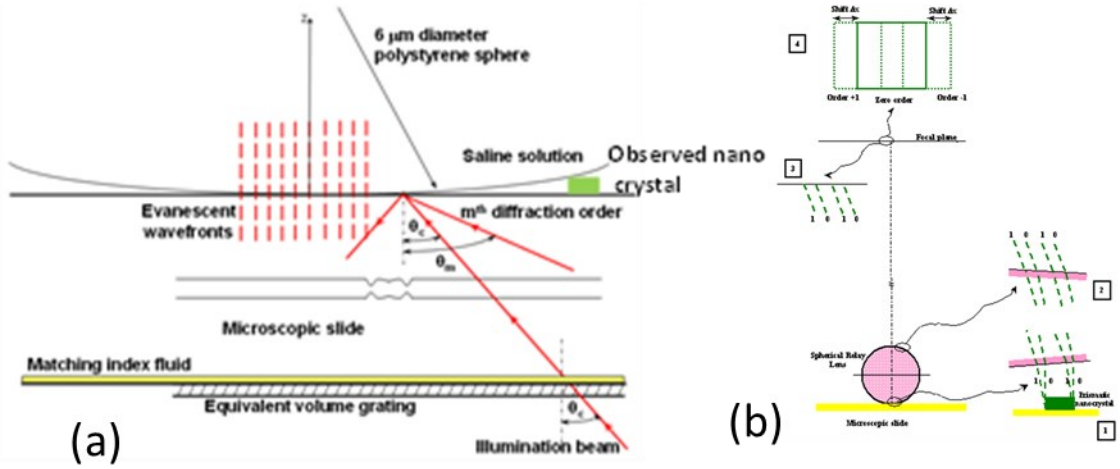

Fig.2. (a) Expanded view of the region of the microscope that contains the observed objects; (b) Schematic representation of the optical circuit forming the image.

In [3], the basic foundations of the data gathering and processing of the nano-microscope were outlined and illustrated with examples of the work done by the authors in preceding work utilizing prismatic nano-crystals and nano-spheres. In the next sections, very important additional informationwill be introduced providing a broader and more comprehensive information on the proposed methodology.

2. The acousto-optic effect

The acousto-optic effect [4-6] is similar to the photoelastic effect in the sense that the optical permittivity **ε** of a material is changed due to strain components ε_{ij} caused by the propagation of an acoustic wave in the material. It deals with the interaction of light waves with acoustic waves propagating in a given medium.
The equivalent of a diffraction grating moves with the velocity of the sound in a given medium. This diffraction grating acts as phase grating. The mechanical waves produced in a certain medium are resonance effects caused by the electromagnetic field of the evanescent wavefronts. The electromagnetic field causes atomic planes to vibrate. There is a transfer of energy from the mechanical waves to the electromagnetic waves. The model introduced by Brillouin consists of rows of identical atoms separated by a distance d, atomic distance property of the atomic structure of the crystal. The crystal vibration is dynamically determined by the eigen modes of vibration of the crystal,Fig. (3). Brillouin [5] derived this model derived based in the Bragg's scattering equation, Fig.3(a). Fig. 3(b) illustrates the axial mode of vibration of a sodium crystal; the crystal can vibrate in this mode along any of the three axis of the crystal.

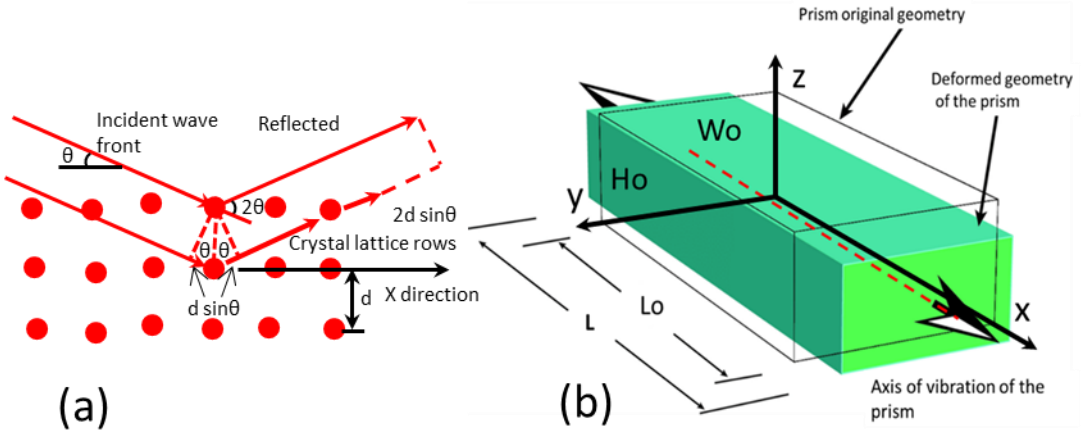

Fig. 3. (a) Bragg's reflection; (b) Sodium crystal'seigenmode of axial vibration.

From Fig. 3(a), the following equation is obtained,

$$\sin\theta_n = n\frac{\lambda}{2\Lambda} \quad (1)$$

Where: λ is the wavelength of the optical wave in the medium under observation, Λ is the wavelength of the acoustic wave, n is the diffraction order of the light, and θ_n is the glancing angle that the incoming ray makes with the reference coordinate system.
An important consequence of the adopted model is that the light wavelength emitted by a crystal is function of the length of the crystal and hence of the number of atoms in the crystal rows since $L_o=N_ad$, where N_a is the number of atoms.Fig. 4 shows the correlation of the wavelength of the emitted light by the crystals and the number of atoms in row. The function $N_a=f(\lambda)$ correlates well with an exponential, $Na=95{,}621e^{-0.0017\lambda}$ with $R^2=0.996$. The model predicts also that there is lower limit in the number of atoms in a crystal that will cause the crystal to emit light.

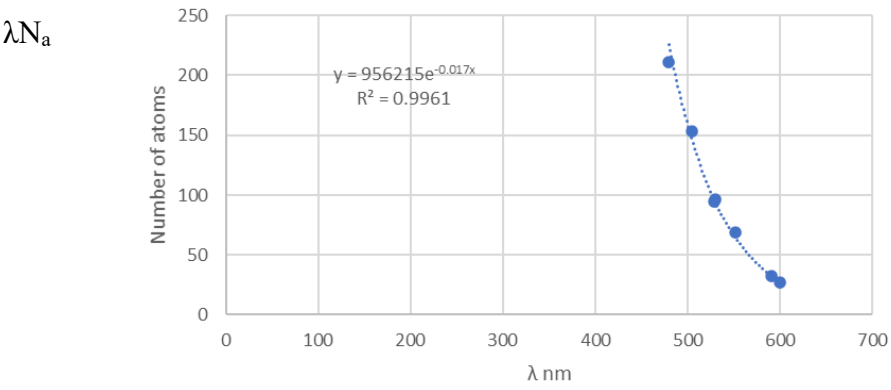

600	27
591	32
552	69
530	96
529	95
505	153
480	211

Fig. 4. Plot of the number of atoms in a crystal vs. the wavelength λ of the emitted light (λ wavelength in nm, N_a number of atoms).

From the preceding analysis the light emission takes place from N_a of the order of few 10's of atoms to about $N_a \approx 250$. Since the emission of light is connected to the eigen modes of vibration of a crystal and the emission depends on the eigen modes frequency, the emitted light wavelength is geometry dependent; different geometries will emit different wave lengths.

3. Carrier fringes that encode spatial information

In [3], and included references itisstablished that utilizing the self-emission of light it is feasible to get optical resolutions in the order of magnitude of fractions of nanometers. A clue of the source of illumination required to observe nano-objects with high spatial resolutions comes from references [7,8]. Originally,Toraldo di Francia [9] developed a theory to increase resolution of images utilizing Bessel beams. In [7,8], experiments were carried out with microwaves to experimentally verify Toraldo di Francia's theoretic developments. To get metrological information from the generated wavefronts, it is necessary to introduce carrier fringes with pitches in the nanometer range. To achieve this task, a method outlined by Toraldo di Francia [10] was adopted. Carrier gratings are introduced in the optical system. A grating illuminated by an evanescent field of light has not only discrete diffraction orders but also evanescent diffraction orders. For these evanescent orders the following equation applies,

$$\sin\theta_n = \frac{\lambda_r}{p_n} \quad (2)$$

In Eq. (3),θ_n is the angle shown in Fig.3, λ_r is the wavelength of the light propagating in the medium of index of refraction n_r, $p_n=p_o/N$, where p_o is the pitch of the grating introduced in the optical circuit (Fig.1) and N is the N-th other of diffraction that has been selected in the FT of the observed image.

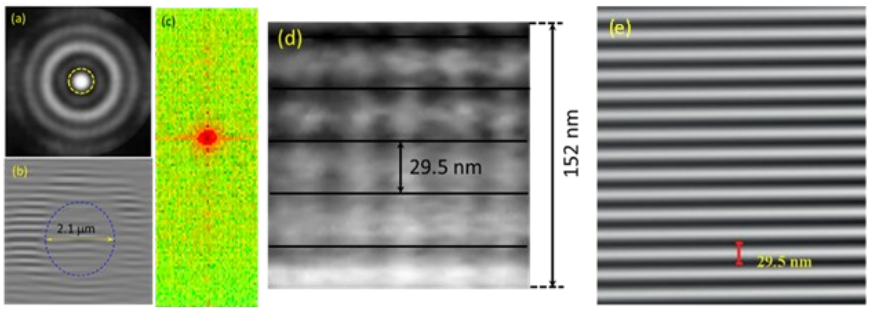

Fig. 5. (a) Region where thenano-images are observed (dashed yellow circle);(b) Carrier fringes modulated by the ball lens;(c)FFT of the region of 2.12 µm diameter;(d) Reference pitch p_o obtained from the FFT of Fig. 5(c);(e) Filtered order p_o.

As shown in[3], all the measurements are carried out in the 2.12 µm diameter region.Fig. 5 illustrates how p_n is obtained. The value of N is selected taking into consideration the ratio ofsignal to noise content in the order, this ratio limits how high N can be selected.

4. Images spatial information decoding

To clarify the process of decoding information, one can get an insight going to the different steps involved in this process. In Fig.3(b), a prismatic nano-crystal is depicted. In a single prismatic crystal,there are three geometrical unknowns, the length L_o, the width W_o, and the height H_o. It is necessary to formulate at least three independent equations that relate recorded images to these unknowns.

Fig. 6(a') shows the images of the upper face of a prismatic nano-crystal. The camera records 3 shifted images: Fig. 6(b') shows recorded images of four nano-crystals. It is necessary to explain why the camera records 3 shifted images.

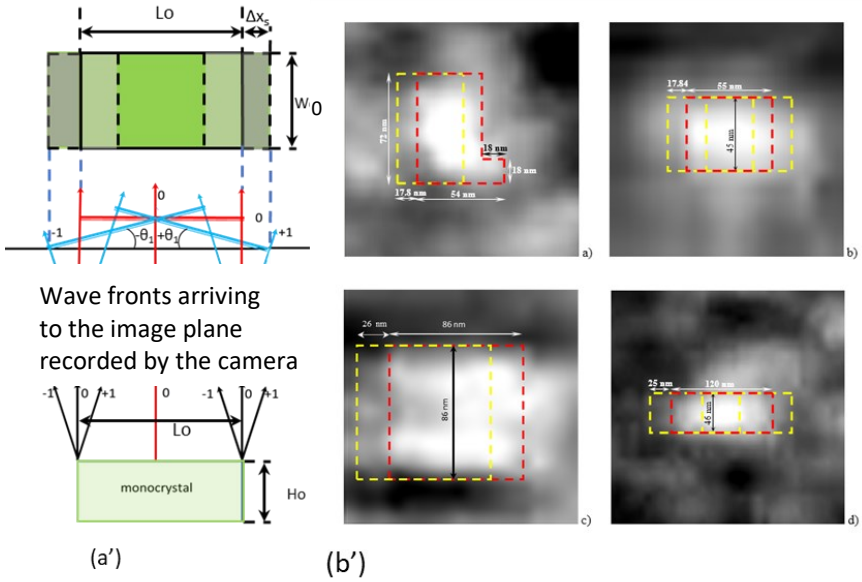

Fig. 6. (a'). Graph illustrating the formation of the observed image caused by the superposition of the three orders, zero order and the±1 orders;(b')Edge detection process for obtaining main geometric dimensions of NaCl nanocrystals: a) L_o=54 nm; b) L_o=55 nm; c) L_o=86 nm; d) L_o=120 nm.

Fig. 7 shows the stationary phase grating generated by the ultrasonic wave propagation in the crystal and emitting light as explained in Section **2**. The order zero emits wavefronts with a normal perpendicular to the upper face of the crystal.

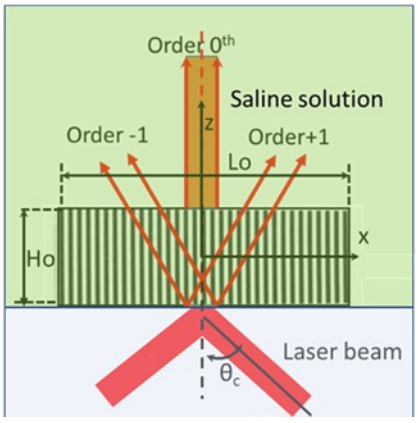

Fig. 7.Orders emitted by the nano-crystal due to the acoustic-optic effect.The ordersN=±1 make the angle θ_1 with respect to the normal of the crystal upper face.

Fig. 7 shows the directions θ of the normals of the orders ±1, these are the angles that appear in Eq.(1). The major energy in the image is held in these 3 orders.
The following relationship connects the shift Δx_s, the angle θ_1 and L_o,

$$tg\ \theta_1 = \frac{\Delta x_s}{Lo} \quad (3)$$

From Eq.(2), for N=1,

$$\Lambda = \frac{\lambda}{\sin\theta_1} \quad (4)$$

The spatial frequency f_e of the ultrasound waves in the nano-prism is:

$$f_e = \frac{\sin\theta_1}{\lambda} \quad (5)$$

The values of L_o, Δx_s, and λ are quantities that are measured from the recorded images. The index of refraction of the medium where the waves propagate,n_r, can be obtained from the literature.Using the adopted model, the measured quantities, and the values of n_r one obtains the relationship between the number ofatoms using the relationship $L_o=N_a\times$dand the frequency of the ultrasound waves, Fig. 8. Theoretically the smallest observable wavelength is $\Lambda\approx 2d$, for the sodium chloride,$\Lambda=2\times0.564$ nm=1.128 nm and the corresponding frequency $f_e\approx$ 0.8865 1/nm, a minimum frequency. The observed frequencies values should be $f_{eo} \geq 0.8865$ 1/nm, the frequency increases with the number of atoms, this trendis shown inFig. 8; the maximum frequency is $11.19\text{x}10^{-4}$ 1/nm. Experimentally and according to the adopted model as the number of atoms increases beyond some number, the prisms do notlonger emit light, the frequency of the emitted light becomes zero, hence in between there must be a maximum frequency as shown in Fig. 8.
From the developments of the preceding paragraphs, it is possible to conclude that the three images seen in the camera image plane are not due to optical diffraction but are produced by the acoustic optic effect. Then, as it is shown in Fig.6, the values of L_o and W_o can be obtained directly from the recorded images.

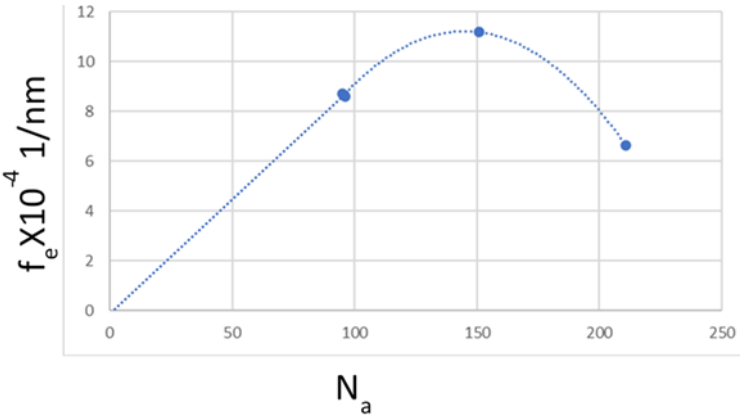

Fig. 8.Correlation of the frequencies of the ultrasound waves in the prismatic crystals and the number of atoms in the crystal's rows.

In [2], the process to get depth information from bodies transparent to a given wavelength is addressed. Looking to Fig. 7,it is possible to point out to two facts: (1) the crystal is enclosed in a saline solution; (2) the normals of the emitted wave fronts by the saline solution and the prism are perpendicular to the plane of the supporting slide. The change of optical path experienced by the zero orders is given by the integral,

$$\delta_{op}(z)=\int_0^{Ho}\left[n_i - n_o\right]dz \quad (6)$$

Converting the difference of optical path to difference of phase one obtains,

$$\Delta\phi(Ho)=\frac{2\pi}{p_m}H_0-\frac{2\pi}{p_c}H_0=\phi_m-\phi_c \quad (7)$$

In Eq. (7), ϕ_c is the phase of selected carrier fringes of pitch p_c, ϕ_m is the phase of the modulated carrier,p_m is the pitch of the modulated carrier that contains the information of the change of optical path as the wavefront goes through the prism.
The preceding analysis is based in a very important property the optical setup shown in Fig. 1. The designed optical arrangement creates locally in the region of observed nano objects a laser-like optical resonator;the illuminating laser provides the energy that feeds the resonator.

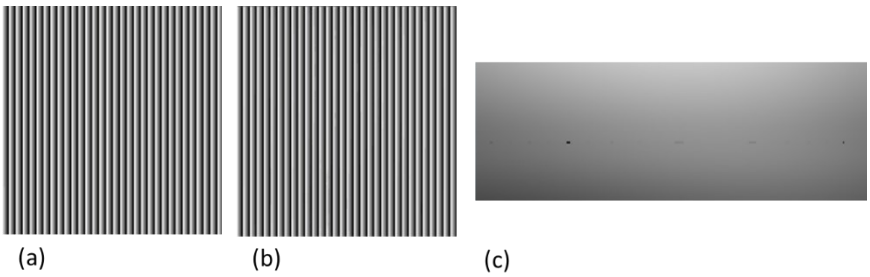

Fig. 9. Phase determination for the nanocrystal of length L=120 nm: a) Reference phase of the carrier fringes p_c=5.53 nm; b) Phase of carrier fringes modulated by the nanocrystal; c) Phase difference in the region of the nanocrystal represented in levels of grey.

Fig. 9 illustrates the procedure utilized to obtain the depth of the crystal of length L_o=120 nm. It is difficult to get the phase of the crystal parallel to the camera plane. Infinitesimal rotation corrections are introduced to remove this effect.
Another example of this approach is given in Fig. 10.

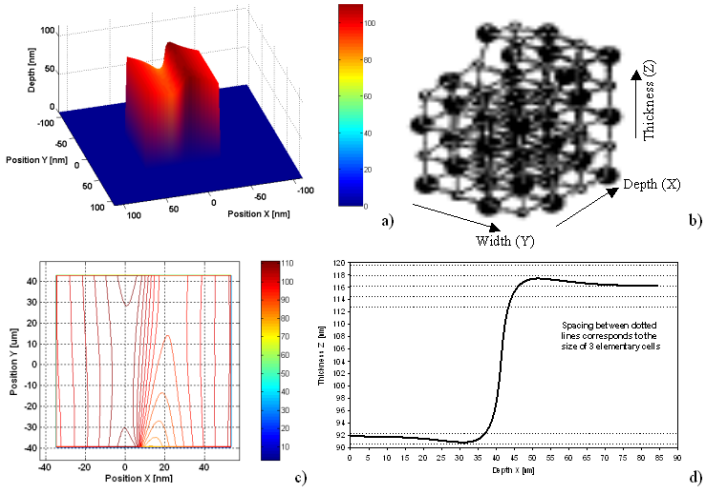

Fig. 10. (a) Reconstruction of the NaCl nanocrystal of length 86 nm; (b) Theoretical structure; (c) Level lines; (d) Rotated cross sectionof the upper face of the nanocrystal: the spacing between dotted lines corresponds to size of three elementary cells.

Applying the outlined decoding procedures, it is possible to get the dimensions L_o, W_o and H_o of the analyzed nanocrystals.Since these dimensions are known form theoretical considerations [11], an estimate of the achieved accuracy with the developed methodologies can be obtained. In Table I, the studied crystals are labeled according to their lengths L_o. For each crystal,are given the measured dimensions, the theoretical dimensions, and the corresponding differences. In the case of the crystal of L_o=86 nm, the jump between the two faces is utilized to get the difference between the measured values and the theoretical values. The mean value for the population of difference readings is Mean=0.082 nm and the standard deviation is STD=±2.06 nm. Roughly, an accuracy of ±3 nm has been achieved.

Table I. Measured dimensions of observedNaCl nanocrystals and comparison with theoretical values.

Crystal Length(nm)	Dimensions Measured(nm)	Dimensions Theoretical (nm)	Difference
Wo	72.0	66.3	+5.7
54	54.0	53.0	+1.0
Ho	53.0	53.0	0.0
Wo	55.0	55.8	-0.8
55	55.0	55.00	0.0
Ho	33.5	33.5	0.0
Wo	86.0	86.0	0.0
86	86.0	86.0	0.0
Ho	----------	--------	-2.38
Wo	46.0	46.0	0.0
120	120	122.7	-2.7
Ho	46.0	46.0	0.0

5.Fourier transform of a Fourier transform

A very important procedure to add to the preceding developments in the process of signal decodingis derived from a property of the FT.A function f(x) has a Fourier transform$F_T(f_{ex})$, wheref_{ex}=1/x.Suppose that one wants to find F(x), a function that is related to f(x) but has very important additional information concerning the analyzed signals.Let us remember thatspatial variable is x whilef_{ex}relates to reciprocal spaces. The function F(.) is a function that can be either in the frequency space or in the coordinates space. In [12], it is shown that, if one calls F_T[f(x)] the FT of f(x), the following relationship is valid,

$$F_T\left[F(x)\right] = f(-f_e) \quad (8)$$

The meaning of the FT of a FT for simplicity of notation is presented in 1D,it can be generalized for more dimensions.

To get the meaning of the preceding derivations,Eq.(8) is applied to the crystal of L_o=86 nm, Fig.11.

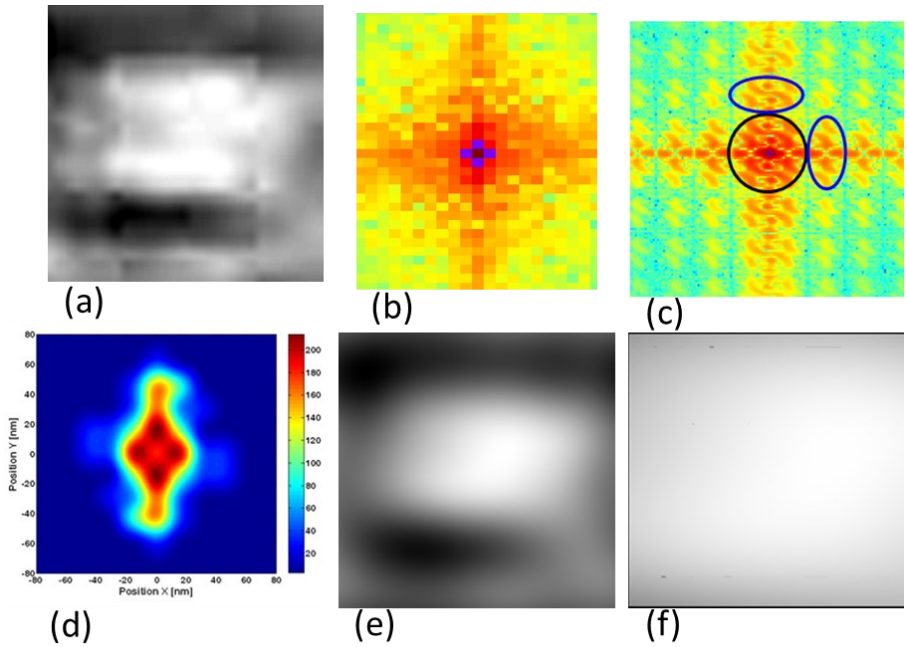

Fig. 11.Nanocrystal of length 86 nm: (a) Grey-level image; (b) FT of (a);(c)FT of the real part of the FT of (a);(d)

Filtered and inverse zero order of (c) (region outlined by black circle); (e) Zero order of image (a); (f) Masked region of (e) corresponding to the crystal size.

In Fig. 11(c),are shown the filters utilized to extract information from the real part FT of the FT. Filtering with the filter outlined with a black circle and taking the inverse transform,one gets the pattern shown in Fig. 11(d). The spatial frequencies displayed in Fig. 11(c) provide information on the distribution of intensities in the image plane x-y. In Fig. 11(c), there are a total of 7 peaks. The two peaks farther apart along the y-axis correspond to a system of horizontal fringes that are in the background of the image and have a pitch p=43.5 nm and do not contain information on the analyzed crystal. The corresponding fringes can be seen in Fig.11(a),and alsoin Fig. 11(e). There are also five additional peaks, one in the center of coordinates that corresponds to the zero order of the pattern. There are four other peaks corresponding to orders ±1 in the X-direction and orders ±1 in the Y-direction, filters outlined in blue ellipses.

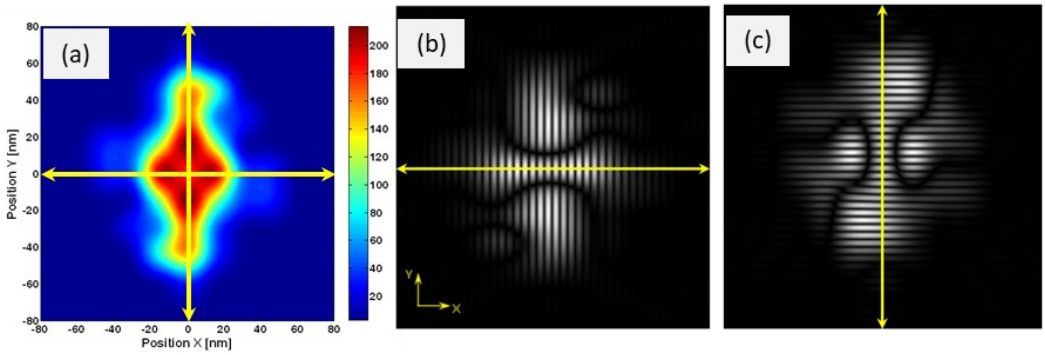

Fig. 12.(a) Inverse transform obtained filtering the zero order provides the intensity distribution in the x-y plane;(b) Filtering the orders ±1 (horizontal blue circles in Fig. 11(c) and inverting we get the carrier fringes that provide the intensity distribution in the x-direction;(c) Doing the same operation with the orders ±1 in the y-direction we obtain the carrier fringes that give the intensity distribution in the y-direction.

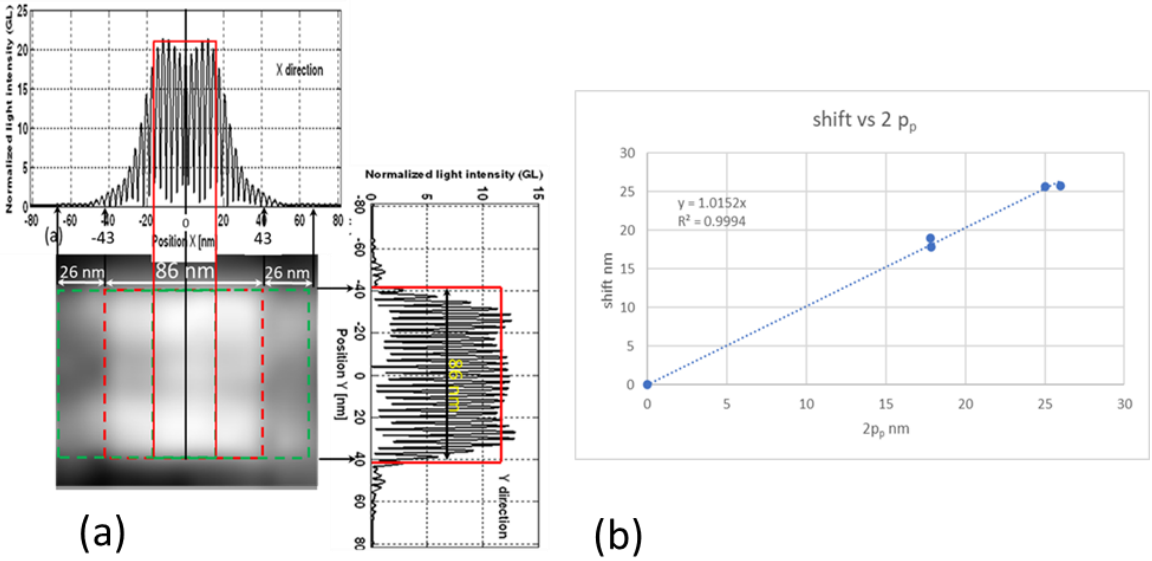

Fig. 13. (a) Image of the crystal of L_o=86 nm, pulses on the x-direction and y-direction;(b) Δx_smeasured with edge detection vs. coordinate x=p_p of the orders ±1 of Fig. 11(d).

Fig.13 integrates the signals thatprovide intensity distribution in the recorded images of the crystal. The upper plot represent 3 rectangular pulses of different intensities. A central rectangular pulse of width W_o=86 nm, and 2 shifted pulses with the shift Δx_s=26 nm. The lateral plot represents one rectangular pulse of width 86 nm. Because of the

orientation of the laser illumination the shifts take place only in the x-direction and there are not shifts in the y-direction. The pulses are encoded in carrier fringes of pitch p=2.91 nm.
Fig.13(b) demonstrates that the shift can be measured independently of the edge detection method utilizing the relationship $\Delta x_s = 2p_s$ where p_s is the coordinate of the horizontal peaks of Fig. 12(a).

6. Metrology of spherical nano-objects

In the preceding sections, the metrology of nano-objects focused on prismatic nanocrystals. In this section, the same methodology applied to nano-prismsis applied to nano-spheres. The analyzed nano-spheres are made out of polystyrene. The nanospheres have a molecular structure quite different from the sodium nano-crystals as polystyrene is an organic material. Thenanospheres are located in the same optical field where the nano-crystals are situated.
Micro/nano-spheres and nano-shells made of dielectric materialsare excellent optical resonators. Of particular interest are vibration modes localized on the surface of the spherical shape. These modes occur at thin ring located on the equator of a sphere or a shell. These modes are called*whispering gallery modes* (WGM)**.** WGM result from light confinement due to total internal reflection inside a high refraction index spherical surface immersed in a lower refraction index medium. In these resonances, the light travels a round trip within the cavity with phase matching. The WG modes are included in the Mie's family of solutions for resonant modes in light scattering by dielectric spheres or shells. The WG modes can be also derived from Maxwell's equations by imposing adequate boundary conditions.
Fig. 14(a) illustrates the standing WGM wave of a nano-sphere. In Fig. 14(b), the image of the nanosphere is noisier than the observed images of nano-crystals. The nano-crystals precipitate from a liquid solution in the microscope slide and are attached to the slide surface. The nanospheres were injected in the fluid hence are free to move and are subjected for example to Brownian motion. Fig.14(d) is the color image of the nanosphere, the violet color corresponds to the emitted light by the nanosphere, λ=386 nm that corresponds to UV radiation. The color camera sensor that captured this image was sensitive to this frequency,which corresponds to a peak wavelength of light emitted by polystyrene. Since the nanosphere is transparent, one can see green hues corresponding to sodium chloride precipitates present in the solution where the nanosphereis immersed.

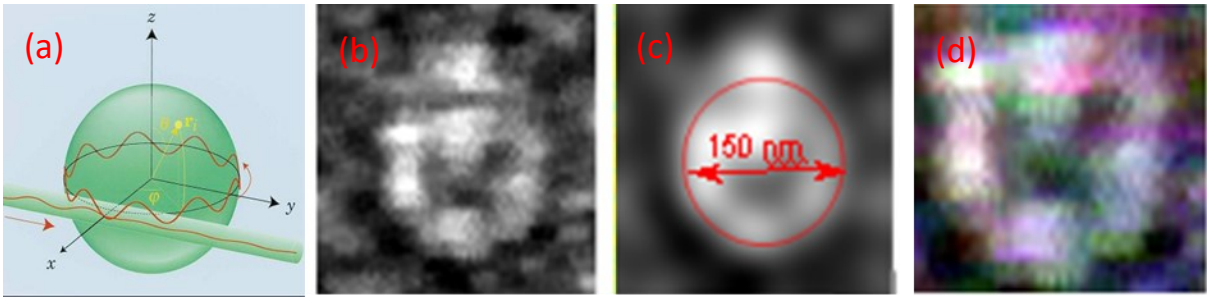

Fig. 14. (a) Standing wave along the equatorial line of a nanosphere; (b) grey level image of a nanosphere;(c) filtered image with indication of the nanosphere's diameter; (d) Color image of the same sphere.

In Fig. 15, data coming from four nanospheresare compared with data numerically obtained from the WGM of a sphere of polystyrene and the same light wavelength [13]. In Fig. 15(a), the equatorial wavelengths $\lambda_{eq}$of the 4nanospheres and the numerical solution for the same wavelength have been correlated with the sphere radiuses. Fig.15(b) shows the variation of the equatorial wavelength of the standing waves divided by the sphere radii with respect the sphere radiuses.
Fig.15(a) provides a linear equation that relates the nanosphere radius R to the equatorial wavelengthλ_{eq},

$$\lambda_{eq} = 0.1051R + 78.612 \quad (9)$$

Applying this equation to the nanosphere of radius 75 nm, replacing R=75 nm in Eq. (9) one obtains, λ_{eq}=86.5027 nm. Since the sphere diameter is 150 nm, the equatorial length isL_{eq}=150nm×3.1416=471 nm, resulting in the ratio L_{eq}/λ_{eq}=471/86.5027=5.4449 ≈5.Hence, there are in total 5 nodes and 5 antinodes, a total of 10.

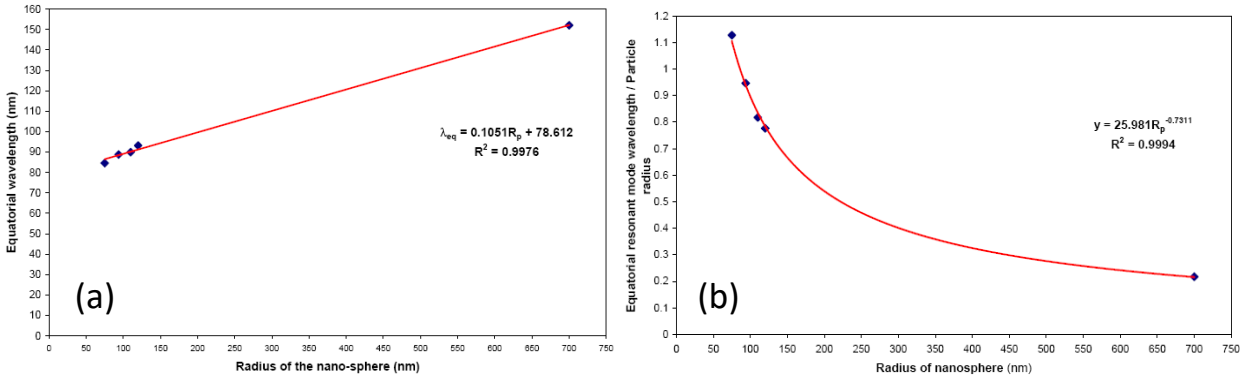

Fig. 15. (a) Relationships between nano-sphere radius R and equatorial wavelength λ_{eq}; (b) Normalized equatorial wavelength of the WGM vs the radiuses of the spheres.

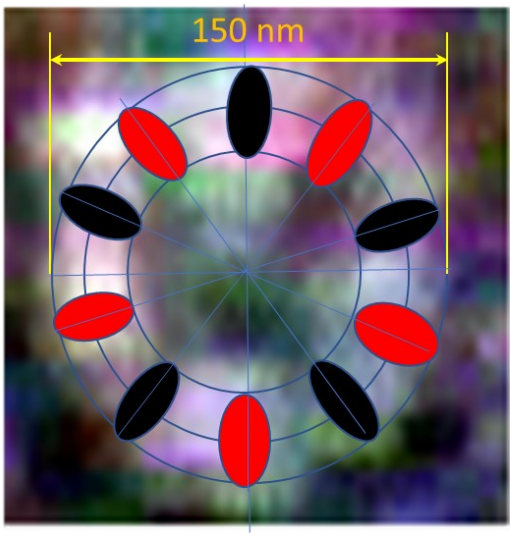

Fig. 16. Image of the nanosphere of diameter 150 nm, nodes(red ellipses) and anti-nodes (black ellipses) corresponding to WGM standing wave.

In Fig. 16, are plotted the nodes and anti-nodes of the sphere of Fig. 14(d). The angle subtended by successive nodes and antinodes is 36°, that is 0.62832 radians. The subtended arc is, 0.62832x75=47.124 nm and since we have a total of 10 arcs, we get L_{eq}=471.24 nm that matches the computed value using Eq. (9).
The image of Fig. 17(c) is the equivalent to the pattern shown in Fig. 11(d) for the nano-prism analysis.

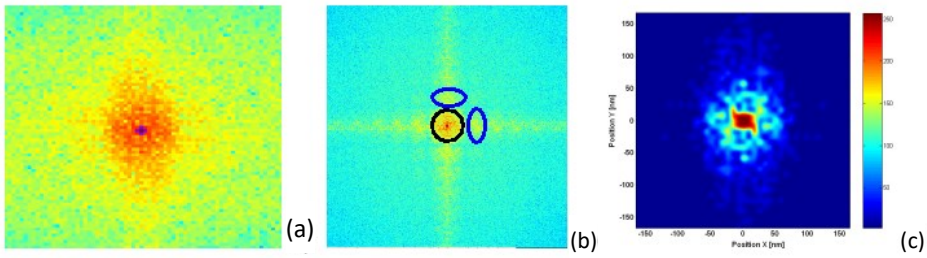

Fig. 17.FT of the image of Fig. 14(b);(b)FT of the real part of (a);(c)Filtered(black filter) and inverse order of(b).

In Fig. 18, the envelopes of the pulses in the x-direction and y-direction are plotted. The curves of Figs. 18(a-b) are the equivalent of the pulses in the x and y-directions of Fig. 17(c). The two profiles are almost identical since there is not shift present in these images.

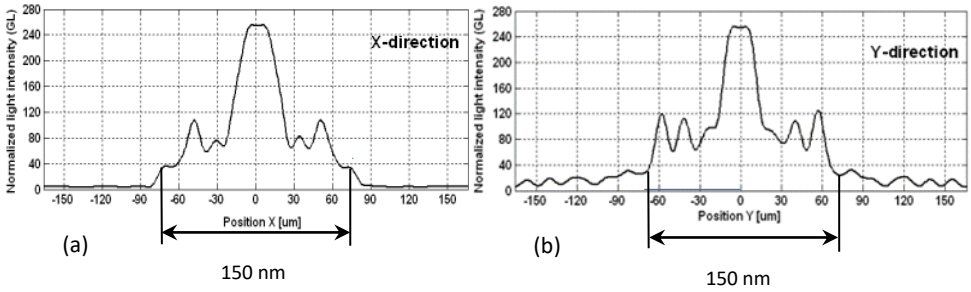

Fig. 18. (a)Cross section of the intensity profile in the x-direction obtained from Fig. 17(c);(b) Intensity profile in the y-direction, filters blue ellipses in Fig.17(b).

Utilizing the circular symmetry of the profiles one can get Fig. 19(a) the loci of maxima intensities, full red circles, and the loci of minimum intensities, dashed circles. The profile of Fig 19(a) is similar to the profiles of Fig. 19(b). The profiles of the Fig. 19(b) were obtained from the pattern of diffraction on the ball lens of D=6μm in [14], reproduced in Fig. 15(c). This means that the intensities distribution in the plane x-y of Fig. 14(d) corresponds to an image formed by the Bessel wavefronts of the sphere of D=150 nm, similar to the distribution of intensities of the much larger sphere of D=6μm. As stated before, this is the same property observed in the nano-prisms.

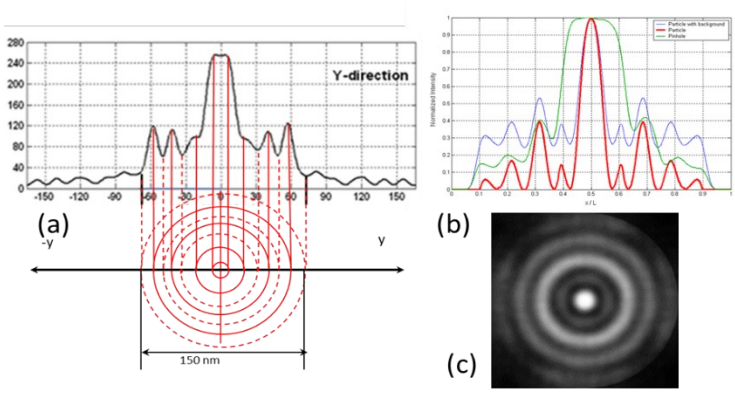

Fig. 19. (a) Nanosphere of D=150 nmand loci of the points of maximum and minimum intensities; (b), (c) Intensity distribution microsphere D=6μm.

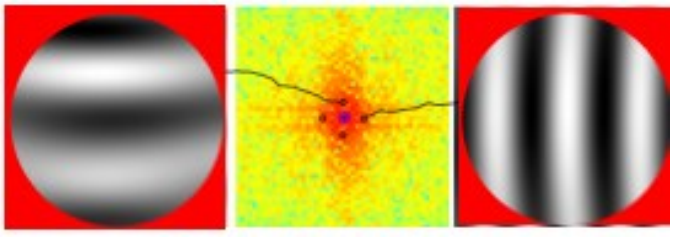

Fig. 20.Fringe patterns corresponding to the sphere of D=150 nm filtered from the FT of Fig.14(b).

The same method of depth determination applied to nanocrystals can be used in the case of nanospheres. In prismatic bodies made of plane surfaces, the interpretation of the decoding process is straightforward. For curved surfaces, the analysis is complex, light beams have trajectories determined by the laws of refraction. Figure 20

shows fringe patterns filtered from the FT of the sphere of Fig.14(b). The analysis of the patterns was performed applying the methodology of the Ronchi test to determine curvatures of lenses. The two patterns gave an average curvature corresponding to the diameter D=150 nm.

From the preceding developments, it can be concluded that, as was previously mentioned, the same methodologies applied to prismatic crystals are valid for nanospheres. The methods utilized for prismatic crystals were based on the acousto-optic effect model of Brillouin. In this model, the medium is made of regular rows of equally spaced atoms. The material of the nanospheres is polystyrene. Polystyrene is a hydrocarbon polymer made from the monomer styrene. It is a long chain organic hydrocarbon. The properties of polystyrene are determined by quite different mutual potentials than the analyzed prismatic nano-crystals. From the results of the performed experiments,these differences do not change the decoding techniques applied to the two set of nano-objects.

This observation has very important implications, the proposed methodology to get high resolution images of nano-objects can be applied to organic materials making it a powerful tool for biosciences.

One important field of application is the monitoring of viruses. Fig. 21 provides an example of this possible application. Fig.21(a) shows a 3D representation of the Covid-19 virus and cross-section. A finite element model of the virus has been developed in ABAQUS, Fig. 21(b). The cover membrane is represented as a thin shell, a hollow spherical resonator. The shell interior is represented as a fluid; the spherical resonator is in a saline solution. The virus spikes are added to the thin shell through a hinge type of connection. The FE model of the virus included about 800,000 elements and nodes. Converge analysis was carried out in order to have a mesh-independent solution. A linear eigenvalue analysis was performed in order to detect natural frequencies and eigen modes compatible with WGM.

The finite element model is shown in Fig. 21(b). Fig.21(c) is a single frame of a movie that shows the vibration of the virus connected to the transformation of mechanical energy into light emission.Spikes do not contribute much to the amplitude of vibration modes. The vibration mode predicted by ABAQUS primarily locates at the equator.

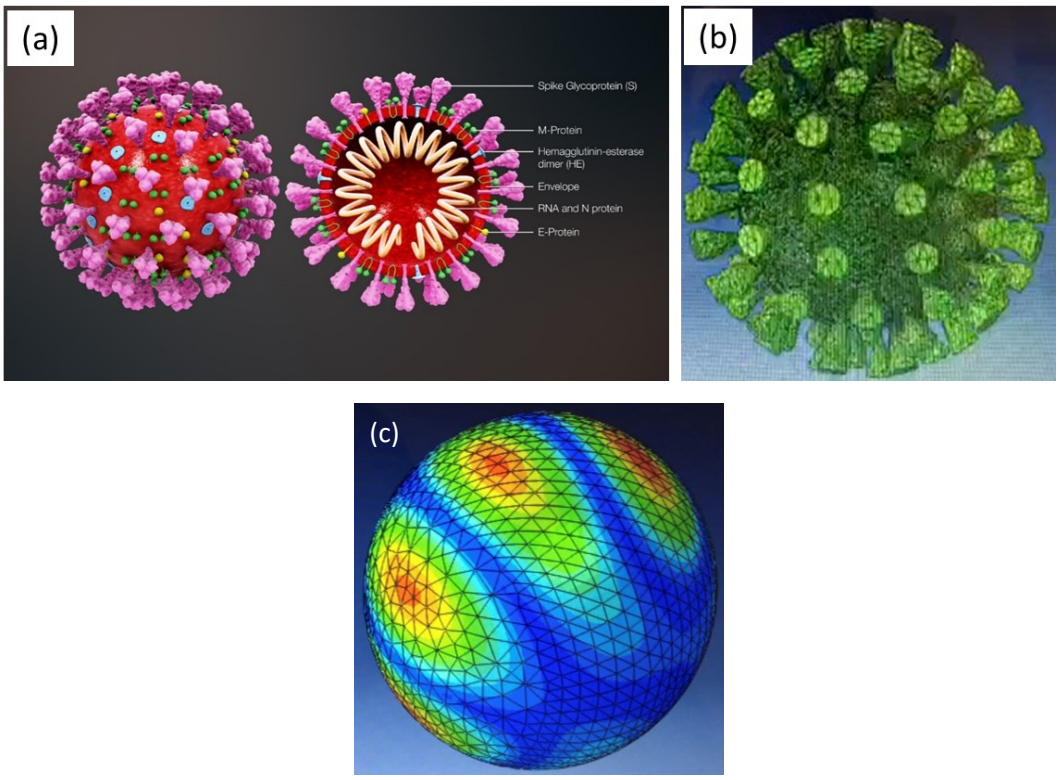

Fig. 21.(a) 3D view of the covid-19 virus and cross-section;(b) Finite element model of the model developed in ABAQUS; (c)One frame of a numerically generated 3D movie of the vibration of the covid-19 virus as a result of the excitation of the virus by light radiation.

7. Conclusions

In the analysis of the mechanisms of infections of living organisms by viruses, imaging technologies play a particularly important role in the process of understanding the virus behavior and the developments associated with the mitigation of the virus effects in humans.

Transmission electronic microscopy(TEM) has been the main provider of static and dynamic sequences showing the mechanisms of interaction of cells and the invading viruses. A TEM has a spatial resolution limits in ranges that produces high resolution images of the viruses interacting with cells. Currently, to observe the images of viruses with TEM requires freezing the viruses at extremely low temperatures. Dynamic pictures of TEM holographic microscopy require a very expensive and complex equipment.

The developments outlined in this paper propose an alternative to accomplish similar tasks to those achieved by TEM at a lesser cost and in environmental conditions that correspond to the normal conditions in living tissues.

Author contribution: *All authors contributed equally to all phases involved the preparation of the article. All authors have read and agreed to the published version of the manuscript.*

References

[1]Sciammarella, C.A., Dichirico, G., Wang, T.C.Moiré-holographic technique for three-dimensional stress analysis. *Journal of Applied Mechanics*1970;37(1):180-185.

[2] Sciammarella C.A.Holographic moiré, an optical tool for the determination of displacements, strains, contours, and slopes of surfaces.*Optical Engineering* 1982;21(3).

[3]Sciammarella C.A., Lamberti L, SciammarellaF.M.Super resolution optical microscopy to detect viruses(SARS-CoV-2) in real time.Proceedings of the Virtual SEM Annual Meeting 2021.

[4]Brillouin, L., Les électrons dans les métaux et le classement des ondes de de Broglie correspondantes. *Comptes Rendus Hebdomadaires des Séances de l'Académie des Sciences* 1930 ;191: 292-294.

[5]Brillouin, L. *Wave propagation in periodic structures*. McGraw-Hill Book Company, New York, USA,1946.

[6]Brillouin, L. Les Tenseurs en Mécanique et en Elasticité, Chapter 3. Vibration des solides et les quanta, pp. 312-319. Masson & C., Paris, France (1949).

[7] Mugnai, D., Ranfagni, A., Ruggeri, R. Pupils with super-resolution. *Physics Letters A* 2003, 311:77-81.

[8]Mugnai, D., Ranfagni, A., Ruggeri, R. Beyond the diffraction limit: super-resolving pupils. *Journal of Applied Physics* 2004;95:2217-2222.

[9] Toraldo di Francia, G. Super-gain antennas and optical resolving power.*Nuovo Cimento* 1952; 9:426-438.

[10] Toraldo di Francia, G. *La Diffrazione della Luce*. Edizioni Scientifiche Einaudi, Torino, Italy,1958.

[11] Hudgins, R.R., Dugourd, P., Tenenbaum, J.N.,Jarrold, M.F. Structural transitions of sodium nanocrystals. Physical Review Letters 1997;78:4213-4216.

[12] Gaskill, J.D.*Linear Systems Fourier Transforms and Optics*, Chapter 7, John Wiley and Sons, New York, 1978.

[13] Pack, A. *Current Topics in Nano-Optics*. PhD Dissertation, Chemnitz Technical University, Chemnitz (Germany), 2001.

[14] Sciammarella,C.A.,Lamberti, L. Sciammarella, F.M.Optical holography reconstruction of nano-objects. In: *Holography, Research and Technologies* (J. Rosen, Ed.), Chapter 9, pp. 191-216. INTECH, Vienna (Austria), 2011.